RSC Advances

PAPER

View Article Online
View Journal | View Issue

Check for updates

Cite this: *RSC Adv.*, 2017, **7**, 56229

Hydrothermal synthesis of $Ba_3Sc_2F_{12}$:Yb^{3+}, Ln^{3+} (Ln = Er, Ho, Tm) crystals and their up conversion white light emission†

Wei Wang, [a] Yunxi Li, [a] Shanshan Hu, *[a] Xuemei Zhang, [a] Jianfeng Tang [b] and Jun Yang *[a]

$Ba_3Sc_2F_{12}$:Yb^{3+}, Ln^{3+} (Ln = Er, Ho, Tm) crystals with various morphologies have been synthesized *via* a one step hydrothermal route. X-ray diffraction (XRD), scanning electron microscopy (SEM), and up conversion photoluminescence (UCPL) spectra were used to characterize the samples. The influences of surfactants, pH values, and molar ratio of F^-/Sc^{3+} on the crystal phase, size and shape of final products have been studied in detail. The aspect ratio of products increased gradually with the increase of F^-/Sc^{3+} molar ratio. Additionally, the luminescence properties of $Ba_3Sc_2F_{12}$:Yb^{3+}, Ln^{3+} (Ln = Er, Ho, Tm) crystals were systematically studied. The blue emission is attributed to the $^1G_4 \rightarrow {}^3H_6$ transition of Tm^{3+}; the green emission can be obtained due to the $^2H_{11/2}/{}^4S_{3/2} \rightarrow {}^4I_{15/2}$ transitions of Er^{3+} and the $^5S_2/{}^5F_4 \rightarrow {}^5I_8$ transition of Ho^{3+}; the red emission comes from the $^4F_{9/2} \rightarrow {}^4I_{15/2}$ transition of Er^{3+} and the $^1G_4 \rightarrow {}^3F_4$ transition of Tm^{3+}. Based on the generation of red, green, and blue emissions in the different Ln ion-doped $Ba_3Sc_2F_{12}$, the white light emission can be obtained by appropriately doping Yb^{3+}, Er^{3+}, and Tm^{3+} in the present $Ba_3Sc_2F_{12}$ crystals due to the color superposition principle. Here, the sample $Ba_3Sc_{1.5856}F_{12}$:$0.4Yb^{3+}$, $0.01Er^{3+}$, $0.0044Tm^{3+}$ crystals showed suitable intensity ratio of blue, green and red (RGB) emissions resulting in bright white light with CIE-x = 0.274 and CIE-y = 0.287, which was illustrated by a photograph under excitation of 980 nm. The prepared $Ba_3Sc_2F_{12}$:Ln^{3+} phosphor has potential applications in the fields of three dimensional displays, back lighting and white light sources.

Received 23rd October 2017
Accepted 7th December 2017

DOI: 10.1039/c7ra11680b

rsc.li/rsc-advances

Open Access Article. Published on 12 December 2017. Downloaded on 6/18/2025 4:16:04 AM.
This article is licensed under a Creative Commons Attribution-NonCommercial 3.0 Unported Licence.

1. Introduction

Luminescent functional materials have been developed for use in the fields of up-conversion luminescence bioimaging,[1] photodynamic therapy[2] and sensing device for antioxidants,[3] such as organic dyes,[4] metal complexes,[5–9] metal nanoparticles,[10] semiconductors[11] and lanthanide-doped inorganic phosphors.[12,13] Most of these ordinary compounds display luminescent emission with a Stokes shift which generates low-energy photons under excitation of high-energy photons; but few processes observe the opposite rule to produce up conversion (UC) photoluminescence with an anti-Stokes shift. The general principle of up the conversion luminescence process can be described as the ground state of the luminescent center absorbing a low-energy photon or being excited to the excited state by a corresponding energy transfer (ET) process, then another low-energy photon is absorbed or an ET process promotes electrons to reach a higher excited state, finally the electrons return to the ground state with emission of high-energy photons. As far as we know, the up conversion luminescence process of lanthanide ions should rely on their rich 4f-electron configuration with abundant energy levels. Lanthanide-doped materials show excellent up conversion luminescence properties including large anti-Stokes shift, long up conversion luminescence lifetime (~ms), sharp lines of emission, low excitation energy (980 nm) and great photostability.[14] In order to minimize the nonradiative loss and maximize the emitted radiation, the desirable host lattice materials should have low phonon energy. This is because the high phonon energy in the host lattice will promote nonradiative energy loss. Oxide exhibits high chemical stability, but their phonon energies are relatively high (>500 cm^{-1}). In contrast, fluoride generally exhibits high chemical stability and low phonon energy (~500 cm^{-1}). Therefore, the fluoride is often used as host material for up conversion process.[15]

To date, various UC matrix materials have been investigated, such as lanthanide oxides,[16,17] fluorides,[18–21] molybdates[22] and vanadates.[23] In recent years, many efforts have been made to synthesize Y/Ln (Ln = La, Ce, Pr, Nd, Sm, Eu, Gd, Tb, Dy, Ho, Er, Tm, Yb and Lu)-based fluorides with controllable crystal phase, shape and size. Nevertheless, Sc-based fluorides hosts have been neglected.[24–28] As we all know, the up conversion

[a]School of Chemistry and Chemical Engineering, Southwest University, Chongqing, 400715, China. E-mail: jyang@swu.edu.cn; hushan3@swu.edu.cn

[b]Faculty of Materials and Energy, Southwest University, Chongqing, 400715, China

† Electronic supplementary information (ESI) available. See DOI: 10.1039/c7ra11680b

Open Access Article. Published on 12 December 2017. Downloaded on 6/18/2025 4:16:04 AM.
This article is licensed under a Creative Commons Attribution-NonCommercial 3.0 Unported Licence.

luminescence depends on the distance between the doped rare earth ions in host lattice. Compared to Y/Ln-based fluorides, Sc-based fluoride is particular because of its atomic electron configuration and smaller ion radius. Thus, the Er^{3+}–Yb^{3+} cation pair is closer in the Sc-based fluoride, which is more effective for energy transfer from Yb^{3+} to Er^{3+} ion.[29] The BaLnF (Ln = Y, La, Ce, Pr, Nd, Sm, Eu, Gd, Tb, Dy, Ho, Er, Tm, Yb and Lu) family has been greatly enriched in recent years.[30–37] Moreover, Lin's group reported that the three-doped $BaYF_5$:Yb, Er, Tm nanoparticles with tunable color upconversion luminescence including the white light;[30] Anthony K. Cheetham and co-operator reported that efficient white light emission by doping Yb^{3+}, Er^{3+} and Tm^{3+} ions in Y_2BaZnO_5 host;[38] our group also reported that the Sr_2ScF_7:Yb^{3+}, Er^{3+}, Tm^{3+} nanoparticles were successfully prepared to obtain white light emission.[39] On the other hand, Fedorov's group reported that the $Ba_3Sc_2F_{12}$ was synthesized using coprecipitation from aqueous solutions;[40] Qnacton's group reported that the $Ba_3Sc_2F_{12}$ was obtained by solid-state method and its structure and unit cell parameters were studied.[41] A method to prepare single phase $Ba_3Sc_2F_{12}$ powders was proposed in these two reports, but there was no discussion about the luminescent properties of $Ba_3Sc_2F_{12}$, especially no UC white light emission.

High temperature solid state method, thermal decomposition, and hydro(solvo)-thermal synthesis are nowadays the three most common routes to prepare RE-based fluorides. The high temperature solid state method is favorable for synthesis of RE-based fluorides compared with the thermal decomposition that requires very toxic fluorinated and oxy-fluorinated carbon species. Although high-quality of RE-based fluorides can be realized in the high temperature solid state method, but it also has some disadvantages including complicated experimental condition, tedious procedure and high reaction temperature. Additionally, the hydro(solvo)-thermal method is more suitable to prepare highly crystalline fluorides nanomaterials under relatively mild condition.[28,42–44]

Compared with the traditional high temperature solid state reaction route, the hydrothermal synthesis of UC fluorides has the advantage of controlled morphology and size, but it loses the high emission efficiency due to the high concentration defects and OH^-. In the past decade, many approaches have been reported to increase the UC emission efficiency of lanthanide-doped nanoparticles, for example, using noble metal nanocrystal plasma,[45] photonic crystal effect,[46] surface coating through core–shell structure[47] and ion-exchange modified hydrothermal method.[48–50]

The Yb^{3+} ions have a larger near infrared (NIR) absorption cross section, which act as an excellent sensitizer codoped with Er^{3+} or Ho^{3+} or Tm^{3+} ions and result in strong red or green or blue UC emissions. Richards' group report near-infrared-to-visible La_2O_3:Yb^{3+}, Er^{3+} (LYE) UC materials with a high internal quantum yield (UCQY) of 3.8%, external UCQY (brightness) of 1.6% and tunable emission color.[51] B. S. Richards[52] and partners respectively discuss the optical property of Yb^{3+}/Er^{3+}, Yb^{3+}/Tm^{3+} and Yb^{3+}/Ho^{3+}. As we all know, UC white light in displays, back lighting and general lighting alternatives have a wide range of applications because it is compact, cheap and power-rich. In order to achieve a combination of RGB emissions in a single inorganic phosphor, it is possible to incorporate Er^{3+}, Tm^{3+}, Ho^{3+} and Yb^{3+} ions into the host material, which is one of the most effective methods to obtaining UC white light.[53–55]

In our report, we prepared $Ba_3Sc_2F_{12}$ crystal by hydrothermal method under mild condition, and researched the effects of surfactants and pH value on the phase and morphology. Furthermore, the molar ratio of F^-/Sc^{3+} has a large effect on the size and aspect ratio of the crystal. We doped Yb^{3+}, Er^{3+}, Tm^{3+} and Ho^{3+} ions in $Ba_3Sc_2F_{12}$ host to achieve tunable multicolor up conversion luminescence from RGB to white light emission.

2. Experimental

2.1 Chemicals and materials

RE_2O_3 (RE = Sc, Ho, Er, Tm, Yb) (99.99%) were purchased from Chuandong Chemical Reagents Company (China), barium chloride dihydrate ($BaCl_2 \cdot 2H_2O$), sodium tetrafluoroborate ($NaBF_4$), trisodium citrate dihydrate (Cit^{3-}), ethylenediamine (EDA), L-glycine (L-Gly), ethylenediaminetetraacetic acid disodium salt (EDTA-2NA), sodium hydroxide (NaOH) and nitric acid (HNO_3) were analytical grade reagents from Aladdin Industrial Corporation (China), and all above materials were used without further purification.

2.2 Preparation

First, the rare earth oxides were dissolved in HNO_3 aqueous solution and removed the excess HNO_3 by evaporation to form $RE(NO_3)_3$ solution for further use. In a typical process for the $Ba_3Sc_{1.59}F_{12}$:$0.4Yb^{3+}$, $0.01Er^{3+}$ nanocrystals: 2 mmol trisodium citrate dihydrate (Cit^{3-}) was dissolved in 30 ml deionized water to form a clarified solution under sustaining magnetic stirring at room temperature. Subsequently, 2 mmol $RE(NO_3)_3$ (RE = Sc, Yb and Er) solution was dropwise added into the aforementioned solution. Then, 3 mmol $BaCl_2 \cdot 2H_2O$ and 4 mmol $NaBF_4$ were added into the antecedent solution respectively. And then, the pH of the mixture solution was adjusted to 11 by adding NaOH solution. Finally, the white precipitate was formed under magnetic stirring for 30 min at room temperature and then transferred into a 50 ml polytetrafluoroethylene autoclave, sealed and maintained at 220 °C for 24 h. As the autoclave cooled to room temperature naturally, the white sediment was separated by centrifugation. It was wished several times with deionized water and ethanol, and dried in air at 80 °C for 12 h to obtain final sample. Meantime, the other $Ba_3Sc_2F_{12}$:Ln^{3+} samples were synthesized *via* similar process.

2.3 Characterization

The crystal structure and phase were analyzed by powder X-ray diffraction (XRD) measured on a Purkinje General Instrument MSALXD3 using Cu Kα radiation ($\lambda = 0.15406$ nm) at a scanning rate of 4° min^{-1} in the 2θ range from 10° to 60°, 20 mA, 36 kV. The morphology of samples was inspected by a field emission scanning electron microscope (FE-SEM, XL30, Philips) operated at an accelerating voltage of 10 kV. The up conversion (UC)

 This journal is © The Royal Society of Chemistry 2017

Open Access Article. Published on 12 December 2017. Downloaded on 6/18/2025 4:16:04 AM.
This article is licensed under a Creative Commons Attribution-NonCommercial 3.0 Unported Licence.

emission spectra were obtained using a 980 nm laser from MDL-N-980-8W as the excitation source and detected by a LS 55 (PerkinElmer) from 300 to 800 nm. All the measurements were performed at room temperature.

3. Results and discussion

3.1 Phase and structure

The pure phase of $Ba_3Sc_2F_{12}$ has been obtained by one step hydrothermal method with trisodium citrate dihydrate (Cit^{3-}). Fig. 1 shows the XRD patterns of $Ba_3Sc_{2(0.995-x)}F_{12}$:$2xYb^{3+}$, $0.01Er^{3+}$ crystals ($x = 0$, 0.05, 0.1, 0.2, 0.3 and 0.4). All diffraction peaks are in good agreement with the standard card of $Ba_3Sc_2F_{12}$ (JCPDS 49-1506) while x = 0–0.3, but superfluous diffraction peak exists at $2\theta = 30.417°$ when $x = 0.4$ (seeing the black spot symbol in Fig. 1), which belongs to (214) crystal plane of the $Ba_4Yb_3F_{17}$ phase (JCPDS 44-0956). With the increase of Yb^{3+} concentration from 0 to 0.3, the diffraction intensity of (111) lattice face gradually diminishes until it disappears; and the intensity ratio of (201)/(211) is gradually reduced, which is the same as the case of (212)/(410) but opposite to the situation of (331)/(312). To sum up, Yb^{3+} and Er^{3+} ions were successfully doped into the $Ba_3Sc_2F_{12}$ host lattice without changing the crystal structure of $Ba_3Sc_2F_{12}$ when Yb^{3+} = 0–0.3; but excess phase of $Ba_4Yb_3F_{17}$ existed when $Yb^{3+} = 0.4$. It is worth noting that the XRD peak shift moved toward low 2θ direction with the increase of Yb^{3+} concentration because of lattice expansion,[39,56,57] but it stopped and moved to higher 2θ direction when $x = 0.4$ due to the emergence of new phase (Fig. S1, ESI†). Table S1 (ESI†) provides direct evidence of lattice expansion that the lattice volume of $Ba_3Sc_{2(0.995-x)}F_{12}$:$2xYb^{3+}$, $0.01Er^{3+}$ increases from 499.89 Å^3 to 507.1 Å^3 with Yb^{3+} concentration at x = 0–0.3. But the lattice volume reduces while $x = 0.4$ due to the emergence of new phase ($Ba_4Yb_3F_{17}$).

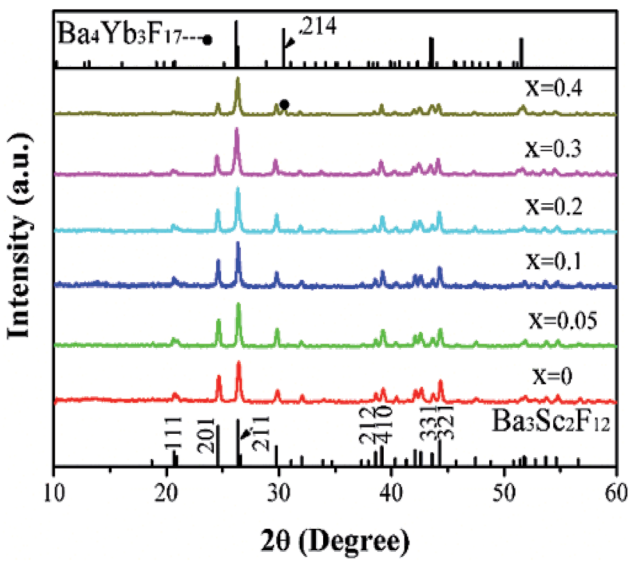

Fig. 1 XRD patterns of $Ba_3Sc_{2(0.995-x)}F_{12}$:$2xYb^{3+}$, $0.01Er^{3+}$ crystals (x = 0, 0.05, 0.1, 0.2, 0.3 and 0.4). The standard data of $Ba_3Sc_2F_{12}$ (JCPDS 49-1506) and $Ba_4Yb_3F_{17}$ (JCPDS 44-0956), respectively.

3.2 Morphology

3.2.1 Effect of surfactant. The XRD patterns and SEM images of the $Ba_3Sc_2F_{12}$ samples with different surfactants are shown in Fig. 2. As displayed in Fig. 2a, all the diffraction peaks can be ascribed to the pure monoclinic $Ba_3Sc_2F_{12}$ (JCPDS 49-1506) when trisodium citrate dihydrate (Cit^{3-}) and ethylenediamine (EDA) are used as surfactants. But there are more or less extra peaks while ethylenediaminetetraacetic acid disodium salt (EDTA-2NA) and L-glycine (L-Gly) act as surfactants or no surfactant, which correspond to the (200), (220) and (311) lattice facets of BaF_2 (mark in Fig. 2a with black rhombuses symbol). Therefore, the trisodium citrate dihydrate (Cit^{3-}) and ethylenediamine (EDA) could limit the formation of BaF_2. Fig. 2b shows the SEM image of $Ba_3Sc_2F_{12}$ sample without surfactant, which presents a spherical shape with diameter of about 5 μm. It is clearly observed that many small particles gathered into a bigger sphere for reducing surface energy. Fig. 2c shows the SEM image of $Ba_3Sc_2F_{12}$ sample with Cit^{3-}, which presents decentralized, uniform and regular cuboid with average size of 200 nm in width and 300 nm in length. The Cit^{3-} was regarded as excellent chelating agents in our work. It could selectively absorb on the specific crystal facet of $Ba_3Sc_2F_{12}$ which slow down the nucleation as well as avoid nanocrystals agglomeration leading to subsequent further grow into the cuboid particle.[58,59] Fig. 2d shows the SEM image of $Ba_3Sc_2F_{12}$ sample with EDA, which presents a spherical shape with diameter of

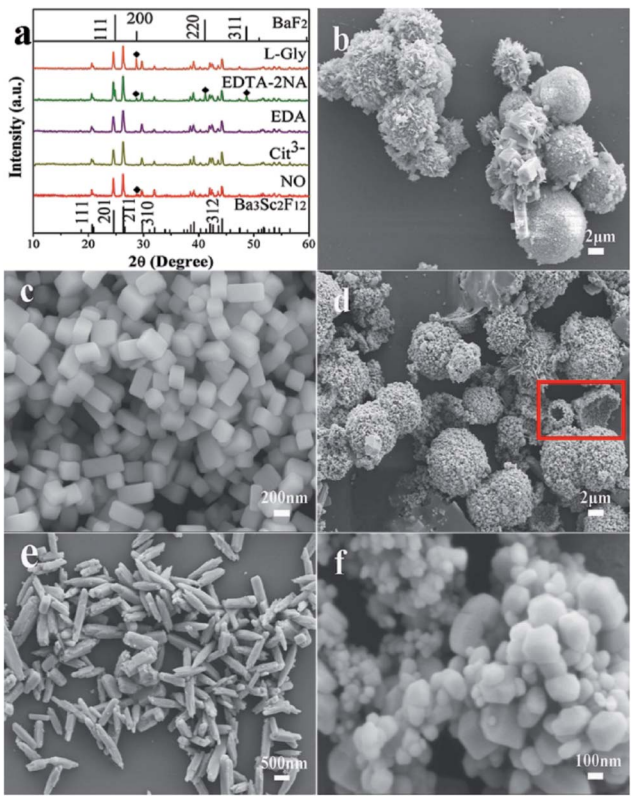

Fig. 2 XRD patterns of the $Ba_3Sc_2F_{12}$ crystals with different surfactants (a) and the corresponding SEM images ((b) NO; (c) Cit^{3-}; (d) EDA; (e) EDTA-2NA; (f) L-Gly).

Open Access Article. Published on 12 December 2017. Downloaded on 6/18/2025 4:16:04 AM.
This article is licensed under a Creative Commons Attribution-NonCommercial 3.0 Unported Licence.

about 5 μm assembled by many smaller nanoparticles. It is interesting that these spheres may be hollow spheres from the of view of individual incomplete sphere in Fig. 2d (seeing the red mark). Fig. 2e shows the SEM image of $Ba_3Sc_2F_{12}$ sample with EDTA-2NA, which presents spindles with length of about 1 μm. Fig. 2f shows the SEM image of $Ba_3Sc_2F_{12}$ sample with L-Gly, which presents nanoparticles with uneven size from 50 to 200 nm. In summary, Cit^{3-} is most suitable to be a surfactant for preparation of disperse, uniform and regular product with pure phase in our present experiment.

The morphology of crystal is influenced by internal crystallographic structure and external growth environment. Once the crystalline structure is determined, the characteristic unit cell of the seed dramatically influence the further crystal growth.[60,61] The $Ba_3Sc_2F_{12}$ belongs to tetragonal in syngony, and its seed has an anisotropic unit structure which can induce anisotropic growth along the crystal reaction direction to form cube. The Cit^{3-} could attach to the characteristic crystal faces and slow down the nucleation, so that the $Ba_3Sc_2F_{12}$ crystal grew into a rectangular cuboid. The interaction force between different surfactants and individual crystal plane is much different, which will change the relative growth rate of crystal plane and then transform the size and shape of the final crystal.

3.2.2 Effect of pH value. It was found that the pH value of initial reaction solution has a great effect on morphology and size of the $Ba_3Sc_2F_{12}$ crystal. When pH = 5, the morphology of product is decanedron that is truncated octahedron (Fig. 3a). The average size of decanedron is about 6 μm. The size becomes smaller to 2 μm when pH = 7 (Fig. 3b). At the same time, the transformation of geometry from truncated octahedron to tetrakaidecahedron happened because two new crystal facets {010} and {100} have appeared. It is noticed that the {101} plane gradually disappeared while the portion of {100} and {010} planes increased accordingly. Finally, the {101} crystal face completely disappeared, and then the cuboid formed at {100} plane direction with 200 nm and {010} plane orientation with 300 nm when pH = 9–11 (Fig. 3c and d).

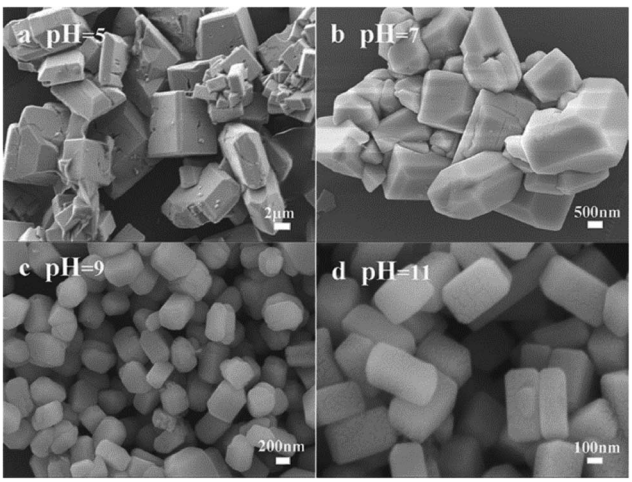

Fig. 3 SEM images of $Ba_3Sc_2F_{12}$ crystals prepared at different pH values.

For the formation of the $Ba_3Sc_2F_{12}$ crystal, the possible process can be proposed as follows:

$$Sc^{3+} + Cit^{3-} \rightarrow Sc^{3+} - Cit^{3-}\ (\text{complex}) \quad (1)$$

$$NaBF_4 + 4OH^- \rightarrow Na^+ + 4F^- + B(OH)_4^- \quad (2)$$

$$3Ba^{2+} + 12F^- + 2Sc^{3+} - Cit^{3-} \rightarrow Ba_3Sc_2F_{12} + 2Cit^{3-} \quad (3)$$

As shown in Scheme 1, the Sc^{3+}–Cit^{3-} complex was obtained when a certain amount of Na_3Cit was added into the initial solution. Under high temperature and high pressure, BF_4^- and Sc^{3+}–Cit^{3-} complex gradually released F^- and Sc^{3+} ions, respectively. Subsequently, they combined with Ba^{2+} in solution to form $Ba_3Sc_2F_{12}$ seed. It has been confirmed that $NaBF_4$ in acidic solution is slowly hydrolyzed to produce $B(OH)_4^-$ and F^- anions in previous reports.[62,63] The slow nucleation rate in solution caused large size of the final product because of the low content of F^- and Sc^{3+} ions under faintly acid condition (pH = 5). The Cit^{3-} selective absorb onto the {001} plane which has lower surface energy than the {101} plane, consequently prevent the enlargement in the {001} plane direction and accelerate the growth along the {101} crystal plane. So it is shown in Scheme 1 that the {001} crystal face is much larger than {101} plane. The pH value can directly affect the bonding strength of Sc^{3+}–Cit^{3-} complex and also affect the surface energy of crystal facets.[64] The concentration of Sc^{3+} and F^- ions increases because the bonding force of Sc^{3+}–Cit^{3-} complex is weakened and the hydrolysis of BF_4^- ion is enhanced with the increase of the pH value from 5 to 11, which will accelerate the nucleation process and be conducive to the production of small size product. When pH = 7, two new crystal faces {010} and {100} began to appear and the {101} crystal faces began to decrease. Finally, the {101} crystal planes disappeared to form a cuboid crystal when pH = 11. It illustrates that the {101} plane has larger surface energy to caused faster relative growth rate until disappearing (Scheme 1).

Based on the above analysis, it is obvious that the pH value can change the bonding strength of Sc^{3+}–Cit^{3-} compound and the content of F^- ions, and thus affect the size of the crystal. Furthermore, the pH value can affect the crystal surface energy, and thus affect the relative growth rate of crystal planes, which is related to the shape of crystal. It is obvious that pH value plays an important role on size and shape of the final crystal.

3.2.3 Effect of molar ratio of F^-/Sc^{3+}. The SEM images of $Ba_3Sc_2F_{12}$ obtained at different molar ratios of F^-/Sc^{3+} are shown in Fig. 4a–d, respectively. When F^-/Sc^{3+} = 6 : 1, the resulting $Ba_3Sc_2F_{12}$ sample is cube with length of 200 nm and

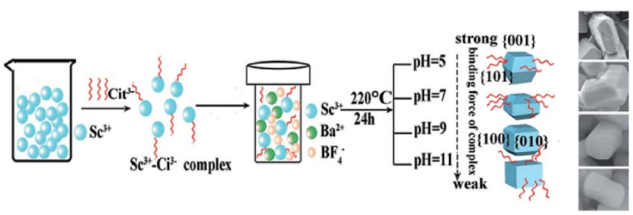

Scheme 1 Schematic illustration for the effect of pH values on morphology of the $Ba_3Sc_2F_{12}$ crystal.

This journal is © The Royal Society of Chemistry 2017

Open Access Article. Published on 12 December 2017. Downloaded on 6/18/2025 4:16:04 AM.
This article is licensed under a Creative Commons Attribution-NonCommercial 3.0 Unported Licence.

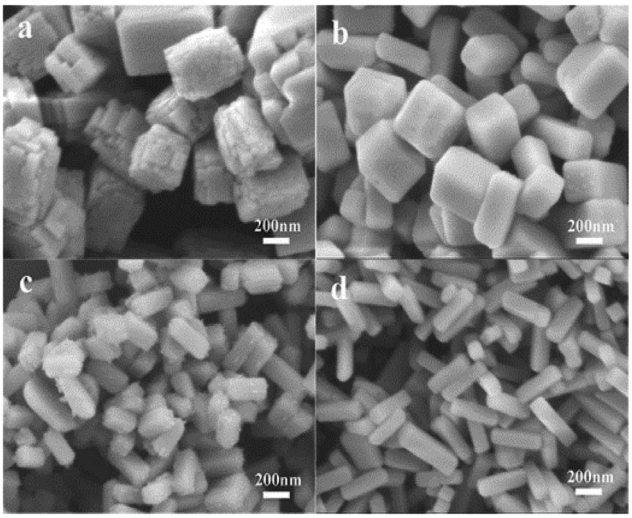

Fig. 4 SEM images of $Ba_3Sc_2F_{12}$ crystals obtained at different molar ratios of F^-/Sc^{3+}: (a) 6 : 1; (b) 8 : 1; (c) 12 : 1; (d) 16 : 1.

aspect ratio of 1 (length/diameter, L/D) (Fig. 4a). It is clearly observed that these cubes are made up of many smaller cubes and the surface looks rough. The rough surface disappears and becomes smooth (Fig. 4b), and also the aspect ratio (L/D) increases because the length increases and width decreases with the increase of the molar ratio of F^-/Sc^{3+}. When F^-/Sc^{3+} = 16 : 1, the length increases to 400 nm and the width decreases to 100 nm. That is to say the aspect ratio increases from 1 to 4 (Fig. 4a and d). Based on the above results, it is reasonable to believe that the molar ratio of F^-/Sc^{3+} has a great effect on both shape and size of the final products. At the early stage, the Cit^{3-} anions were introduced into the reaction system and combined with Sc^{3+} ions to form Sc^{3+}–Cit^{3-} compound through strong coordination interaction.[65] Then under the hydrothermal conditions of high temperature and pressure, the chelating power of the Sc^{3+}–Cit^{3-} compound would be weakened, and slowly released Sc^{3+} ions. Additionally, F^- and Ba^{2+} in the solution react with Sc^{3+} to produce $Ba_3Sc_2F_{12}$ nuclei. The pure crystal of $Ba_3Sc_2F_{12}$ was obtained in the low molar ratio of F^-/Sc^{3+} = 6 : 1, while the size and shape of $Ba_3Sc_2F_{12}$ vary along with the increase of molar ratio of F^-/Sc^{3+} from 6 : 1 to 16 : 1.

This can be explained by different capping effect of F^- ions on different crystal faces, which is similar to the example of the morphology control forβ-$NaYF_4$ in the previous literature.[66] In Gibbs–Thompson theory, the relative chemical potential of the crystal is proportional to its surface atomic ratio, which is determined by the average number of hits per atom on the entire crystal.[67] The cupping effect of F^- ions will decrease the average number of dangling bonds, and further reduce the chemical potential of the crystal plane. The density of Sc^{3+} on different crystal face is diverse. The density of Sc^{3+} on the crystal plane in width direction is greater than that in length direction, which results in the selective absorption capacity of F^- ions on the plane in width direction is greater than that in length direction. So the surface energy of the crystal plane in width direction decreases apace while that of the crystal plane in length direction increases accordingly along with the increase of molar ratio of F^-/Sc^{3+} from 6 : 1 to 16 : 1. As a result, the relative growth rate along the plane in length direction is faster than that in width direction. So, the rod-shaped samples with longer length (400 nm) and higher aspect ratio (L/D = 4 : 1) are formed. The stepped rough surface of cube (Fig. 4a) is formed because the Cit^{3-} slows down the nucleation process and low concentration of F^- ions (F^-/Sc^{3+} = 6 : 1) makes the crystallization incomplete.[39,52,68,69]

3.2.4 Effect of doping concentration. Fig. 5 shows the SEM images of $Ba_3Sc_{2(1-x)}F_{12}$:2$x$$Yb^{3+}$, 0.01$Er^{3+}$ crystals at x = 0, 0.05, 0.1, 0.20, 0.30 and 0.40, respectively. From previous Fig. 1, it is known that the products are pure phase and highly crystalline when x = 0–0.3, but new phase appears while x = 0.4. The cuboid morphology is shown in Fig. 5a, and it is clearly observed that the average size is 200 nm in width and 300 nm in length (x = 0). The crystal growth along length direction grows to around 500 nm when x = 0.05. The length of the crystal increases to 1.5 μm (Fig. 5d) while x = 0.2. However, the crystal growth stop in direction ({100} planes) and maintain size at about 1.5 μm when the Yb^{3+} concentration increases to x = 0.3 and 0.4, but the width of crystal increases with the increase of Yb^{3+} concentration. From the above, the length of the crystal increases from 400 nm to 1.5 μm with the increase of Yb^{3+} concentration from x = 0 to x = 0.2, but the length of crystal was no longer increasing when the concentration of Yb^{3+} was increased to (x = 0.3).

It means that higher doping concentration of Yb^{3+} ions (x < 0.3) is favorable for the anisotropic growth. The reason for that should be related to the different growth rates of the crystals

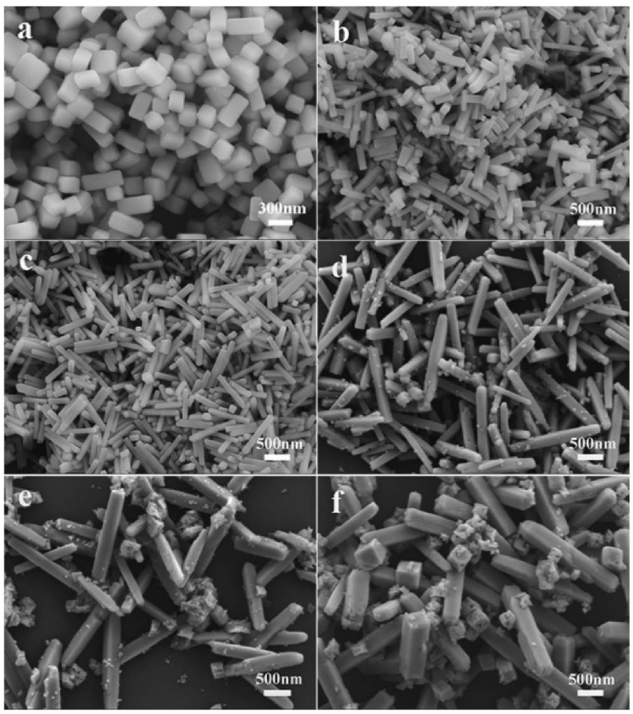

Fig. 5 SEM images of $Ba_3Sc_{2(1-x)}F_{12}$:2$x$$Yb^{3+}$, 0.01$Er^{3+}$ crystals ((a) x = 0; (b) x = 0.05; (c) x = 0.1; (d) x = 0.2; (e) x = 0.3; (f) x = 0.4).

Open Access Article. Published on 12 December 2017. Downloaded on 6/18/2025 4:16:04 AM.
This article is licensed under a Creative Commons Attribution-NonCommercial 3.0 Unported Licence.

along the {100} direction *versus* {001} direction. The greater the concentration ($x < 0.3$), the faster the growth tendency along the {100} orientation; but the further increasing concentration ($x = 0.3$ and 0.4) will inhibit further growth in {100} direction, which is similar to the other case of doping larger-radius lanthanides.[70–72] The lanthanide ions can be doped into the $Ba_3Sc_2F_{12}$ crystal because of the similar radius between Sc^{3+} and other doped ions, as well as the similar Pauling's electronegativity of rare earth ions. The RE^{3+} ions with larger radius replace the Sc^{3+} ions, which would bring a monotonous lattice expansion, and then increase the nucleation energy and restrain heterogeneous nucleation.[56,73] The trisodium citrate dihydrate (Cit^{3-}) is an efficient chelating reagent to selectively adsorb on the {001} crystal planes, and the aggregation of larger-radius RE^{3+} ions on this crystal planes will reduce the concentration of F^- ions, which will result in inhibiting the crystal growth in the {001} direction and faster growth rate in the {100} direction than that in {001} direction. But higher doping concentration ($x = 0.3$ and 0.4) restrains the growth in length direction and promotes the growth in width direction relatively, because the increasing concentration of RE^{3+} with larger radius in {100} direction inhabits the crystal growth in this orientation.[70]

3.3 Up conversion luminescence property

3.3.1 Multicolor light in the $Ba_3Sc_2F_{12}$:Yb^{3+}, Ln^{3+} (Ln = Er, Ho, Tm) system. Fig. 6 displays the up conversion (UC) luminescence spectra of $Ba_3Sc_{2(1-x)}F_{12}$:xYb^{3+}, $0.01Er^{3+}$ crystals with variable Yb^{3+} concentrations from $x = 0$ to $x = 0.3$ under 980 nm laser excitation. Two primary bands in the green emission region with maxima at 520 and 542 nm are attributed to the $^2H_{11/2} \rightarrow {}^4I_{15/2}$ and $^4S_{3/2} \rightarrow {}^4I_{15/2}$ transitions of the Er^{3+} ions respectively, and the wide band in red emission region at 648 nm is ascribed to the $^4F_{9/2} \rightarrow {}^4I_{15/2}$ transition of Er^{3+} ion in $Ba_3Sc_{2(1-x)}F_{12}$:$2xYb^{3+}$, $0.01Er^{3+}$ crystals. The energy required between the ground state and the excited state of Er^{3+} is matched to 980 nm laser.

It is clearly observed that the intensity of green emission reduced but the intensity of red emission enhanced with the increase of the Yb^{3+} ions. A similar result was also observed from some other Yb^{3+}/Er^{3+}-codoped fluorides.[30,39,74–76] The interatomic distance of Yb^{3+}–Er^{3+} in the $Ba_3Sc_2F_{12}$ host lattice would decrease with the increase of Yb^{3+} ions, which would produce two energy-back-transfer processes from Er^{3+} to Yb^{3+} (Fig. 7). The energy-back-transfer of $^4S_{3/2}$ (Er^{3+}) + $^2F_{7/2}$ (Yb^{3+}) → $^4I_{13/2}$ (Er^{3+}) + $^2F_{5/2}$ (Yb^{3+}) (BET1 in Fig. 7) should depopulate the excited levels $^4S_{3/2}$ and $^2H_{11/2}$. So, the green emission ($^2H_{11/2}/{}^4S_{3/2} \rightarrow {}^4I_{15/2}$) decreased.

For the red emission, the mechanism of up conversion emission is predominantly attributed to a two-photons process from the excited Yb^{3+} to Er^{3+} because of larger absorption cross section of Yb^{3+} ions than that of Er^{3+} ions. At first, the ground state $^2F_{7/2}$ of Yb^{3+} absorbed a photon to $^2F_{5/2}$ and then transferred its energy to Er^{3+} ($^4I_{11/2}$). During the lifetime of $^4I_{11/2}$ (Er^{3+}), a second Yb^{3+} ($^2F_{5/2}$) ion transferred its energy again, resulting in the population of the $^4F_{7/2}$ state of Er^{3+}, and then nonradiative relaxation populated the $^4F_{9/2}$ levels, so that the red emission of $^4F_{9/2} \rightarrow {}^4I_{15/2}$ was produced (Fig. 7). At the same time, relaxation from $^4I_{11/2}$ (Er^{3+}) would produce the $^4I_{13/2}$ (Er^{3+}), and then the excited state $^2F_{5/2}$ of Yb^{3+} transfered its energy to Er^{3+} through the energy transfer process $^2F_{5/2}$ (Yb^{3+}) + $^4I_{13/2}$ (Er^{3+}) → $^2F_{7/2}$ (Yb^{3+}) + $^4F_{9/2}$ (Er^{3+}), which can directly populate the $^4F_{9/2}$ red-emitting level (Fig. 7) and increase the red emission at 648 nm with the increase of Yb^{3+} ions.[77] In addition, the energy-back-transfer process of $^4F_{7/2}$ (Er^{3+}) + $^2F_{7/2}$ (Yb^{3+}) → $^4I_{11/2}$ (Er^{3+}) + $2F_{5/2}$(Yb^{3+}) (BET2 in Fig. 7) should restrain the number of electrons on the excited $^4F_{7/2}$ (Er^{3+}) level at higher concentration of Yb^{3+} ions. This would further reduce the population on the green-emitting levels $^2H_{11/2}$ and $^4S_{3/2}$, and then the green emission decreased.[78]

Analyzing the UC emission spectra of $Ba_3Sc_{2(0.995-x)}F_{12}$:$2xYb^{3+}$, $0.01Er^{3+}$ crystals in Fig. 6 and the XRD patterns in Fig. 1, the doping concentration of Yb^{3+} is selected to be 0.2 in $Ba_3Sc_{2(0.995-x)}F_{12}$:$2xYb^{3+}$, Ln^{3+} (Ln = Er, Ho, Tm) crystals for controlling the doping concentration of the total RE^{3+} in proper range (<0.4) to produce the pure phrase of $Ba_3Sc_2F_{12}$. Fig. 8 shows the UC luminescence spectra of Ln^{3+}-doped $Ba_3Sc_2F_{12}$ crystals under 980 nm laser excitation. The $Ba_3Sc_{1.99}F_{12}$:$0.01Er^{3+}$,

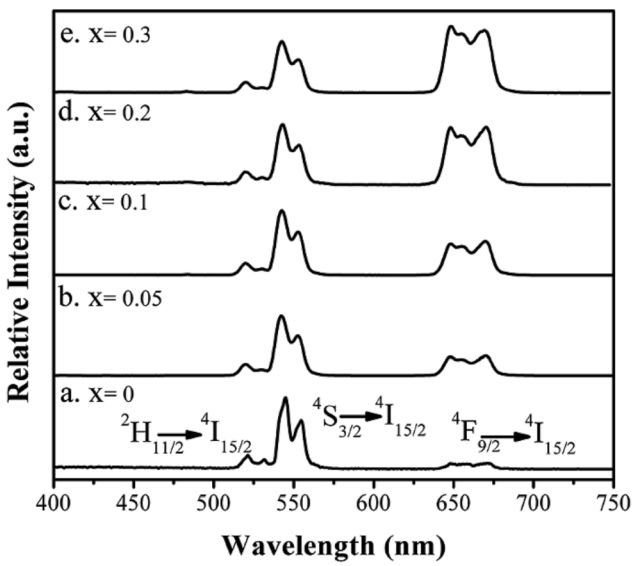

Fig. 6 UC emission spectra of $Ba_3Sc_{2(0.995-x)}F_{12}$:$2xYb^{3+}$, $0.01Er^{3+}$ crystals under 980 nm excitation with power density of 3 W cm^{-2}.

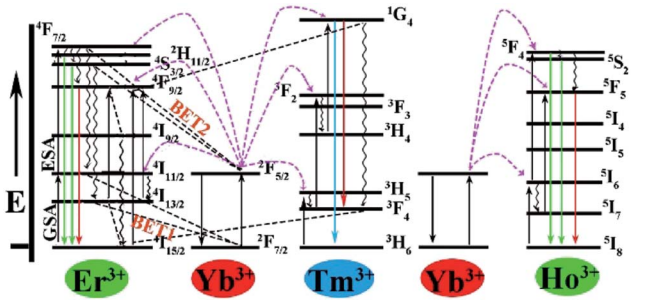

Fig. 7 Energy level diagrams of the Yb^{3+}, Er^{3+}, Tm^{3+} and Ho^{3+} ions and the proposed UC emission mechanism.

This journal is © The Royal Society of Chemistry 2017

Open Access Article. Published on 12 December 2017. Downloaded on 6/18/2025 4:16:04 AM.
This article is licensed under a Creative Commons Attribution-NonCommercial 3.0 Unported Licence.

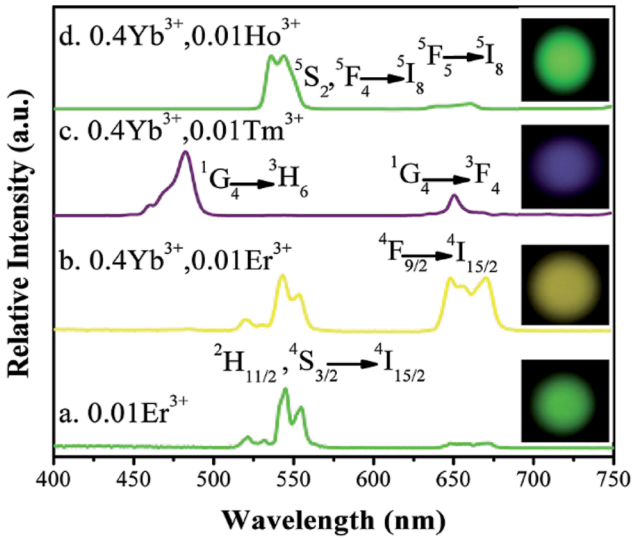

Fig. 8 Up conversion emission spectra and the corresponding luminescent photographs of $Ba_3Sc_2F_{12}$:Ln^{3+} crystals under 980 nm excitation with power density of 3 W cm^{-2} in dark room.

$Ba_3Sc_{1.59}F_{12}$:0.4Yb^{3+}, 0.01Er^{3+}, $Ba_3Sc_{1.59}F_{12}$:0.4Yb^{3+}, 0.01Tm^{3+} and $Ba_3Sc_{1.59}F_{12}$:0.4Yb^{3+}, 0.01Ho^{3+} samples exhibited green, yellow, blue and green emissions, respectively. These color emissions can be confirmed by the corresponding luminescent photographs under 980 nm laser excitation (inset in Fig. 8). The UC emission spectrum of the $Ba_3Sc_{1.99}F_{12}$:0.01Er^{3+} sample excited at 980 nm is shown in Fig. 8a. The green emission is ascribed to $^2H_{11/2}$, $^4S_{3/2}$ → $^4I_{15/2}$ transitions of Er^{3+}; but the red emission region ($^4F_{9/2}$ → $^4I_{15/2}$ of Er^{3+}) was obtained in $Ba_3Sc_{1.59}F_{12}$:0.4Yb^{3+}, 0.01Er^{3+} sample (Fig. 8b), which was mixed with green emission region to show yellow emission. This can be confirmed by the luminescent photograph in Fig. 8b. Fig. 8c indicates that strong blue emission at 482 nm ($^1G_4$ → $^3H_6$ of Tm^{3+}) and weak red emission at 650 nm ($^1G_4$ → $^3F_4$ of Tm^{3+}) respectively, and the $Ba_3Sc_{1.59}F_{12}$:0.4Yb^{3+}, 0.01Tm^{3+} product exhibited blue emission from luminescent photograph under 980 nm laser excitation (inset in Fig. 8c).

Fig. 8d shows the up conversion luminescence spectra of $Ba_3Sc_{1.59}F_{12}$:0.4Yb^{3+}, 0.01Ho^{3+} crystal. The band in the green emission region at 545 nm is attributed to the $^5S_2$, $^5F_4$ → $^5I_8$ transition of Ho^{3+} and the weak red region emission at 663 nm is ascribed to the $^5F_5$ → $^5I_8$ transition of Ho^{3+}. The green emission can be confirmed by the corresponding luminescent photographs under 980 nm laser excitation (inset in Fig. 8d). We can't observe green emission in single Ho^{3+}-doped $Ba_3Sc_2F_{12}$ crystals under 980 nm laser excitation because the ground state absorption (GSA) can't occur, but Yb^{3+} could act as the excellent sensitizer to produce energy transfer process from Yb^{3+} to Ho^{3+} in $Ba_3Sc_{1.59}F_{12}$:0.4Yb^{3+}, 0.01Ho^{3+} crystal, which leads to green emission. As for the red light emission at 663 nm, there are two possible energy ways for the population of the $^5F_5$ red emitting level (Fig. 7): (1) $^2F_{5/2}$ (Yb^{3+}) + $^5I_7$ (Ho^{3+}) → $^2F_{7/2}$ (Yb^{3+}) + $^5F_5$ (Ho^{3+}), in which the $^5I_7$ level is obtained through the nonradiative relaxation from the $^5I_6$ level; (2) nonradiative phonon-assisted relaxation from the $^5F_4$ and $^5S_2$ states to the $^5F_5$ state.[79]

The UC emission property of Yb^{3+}/Er^{3+} and Yb^{3+}/Tm^{3+} will yield the excitation power density because excitation density not only is directly related to the initial population of the excited state in a UC system, but also modifies the multi-phonon non-radiation relaxation probability. To further investigate the emission behavior of Yb^{3+}/Er^{3+} and Yb^{3+}/Tm^{3+} pairs, and the logarithmic relationship of UC emission intensities to power density of $Ba_2Sc_2F_{12}$:0.4Yb^{3+}/0.01Ln^{3+} (Ln = Er, Tm) is shown in Fig. 9. The UC emission intensity increased with power obeying a rule of $I \propto P^n$ for both the green and blue emissions, where I is the emission intensity, P is the excitation laser power density, and n is the number of photons.[80] The n values are obtained to be 1.92 and 3.02 for green and blue emissions, respectively. For the green emission of Yb^{3+}/Er^{3+}, the value of n is close to 2 which indicates that the green emission in $Ba_2Sc_2F_{12}$ matrix is involved in two-photon process; for the blue emission of Yb^{3+}/Tm^{3+} pairs, the n value is close to 3 which indicates that the blue emission in $Ba_2Sc_2F_{12}$ matrix is involved in three-photon process.

Compared with the traditional high temperature solid state reaction route, the hydrothermal synthesis of UC fluorides has the advantage of controlled morphology and size, but it lose the high emission efficiency due to the high concentration defects. We can find that the UC emission intensities of $Ba_2Sc_2F_{12}$:0.4Yb^{3+}/0.01Ln^{3+} (Ln = Er, Tm and Ho) crystals prepared by solid state route are stronger than that prepared by hydrothermal method (see Fig. S2†).

3.3.2 White light in $Ba_3Sc_2F_{12}$:Yb^{3+}, Er^{3+}, Tm^{3+} system. Fig. 10 shows the emission spectra of $Ba_3Sc_{1.59}F_{12}$:0.4Yb^{3+}, 0.01Er^{3+}, $Ba_3Sc_{1.59}F_{12}$:0.4Yb^{3+}, 0.01Tm^{3+} and $Ba_3Sc_{1.58}F_{12}$:0.4Yb^{3+}, 0.01Er^{3+}, 0.01Tm^{3+}, respectively. It is clearly observed that the spectrum of the $Ba_3Sc_{1.58}F_{12}$:0.4Yb^{3+}, 0.01Er^{3+}, 0.01Tm^{3+} is a composite of the spectrum of the $Ba_3Sc_{1.59}F_{12}$:0.4Yb^{3+}, 0.01Er^{3+} and the spectrum of the $Ba_3Sc_{1.59}F_{12}$:0.4Yb^{3+}, 0.01Tm^{3+} (dot line in Fig. 10), in which the blue emission is derived from the $^1G_4$ → $^3H_6$ transition of Tm^{3+} and the green emission is attributed to the $^2H_{11/2}$, $^4S_{3/2}$ → $^4I_{15/2}$ of Er^{3+}. And then carefully

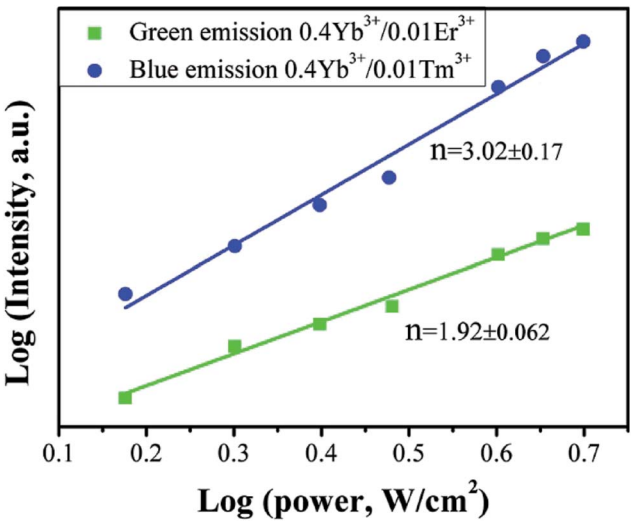

Fig. 9 Double logarithmic relationship of green and blue luminescence intensities *versus* power density of $Ba_2Sc_2F_{12}$:0.4Yb^{3+}/0.01Ln^{3+} (Ln = Er, Tm).

Open Access Article. Published on 12 December 2017. Downloaded on 6/18/2025 4:16:04 AM.
This article is licensed under a Creative Commons Attribution-NonCommercial 3.0 Unported Licence.

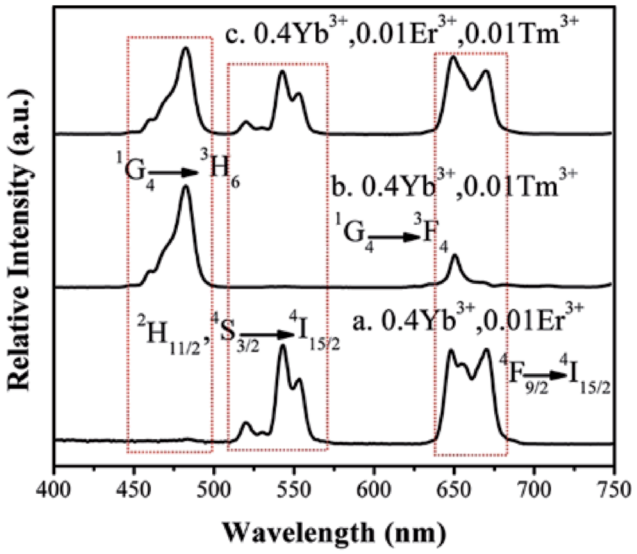

Fig. 10 Up conversion luminescence spectra of $Ba_3Sc_2F_{12}$:Ln^{3+} crystals under 980 nm excitation with power density of 3 W cm^{-2}.

observed, there are three peaks and two troughs in the red area of $Ba_3Sc_{1.59}F_{12}$:0.4Yb^{3+}, 0.01Er^{3+}; however, there were only two peaks and one trough in the red area of $Ba_3Sc_{1.58}F_{12}$:0.4Yb^{3+}, 0.01Er^{3+}, 0.01Tm^{3+} product. It indicted that the red emission of the $Ba_3Sc_{1.58}F_{12}$:0.4Yb^{3+}, 0.01Er^{3+}, 0.01Tm^{3+} is composed of the $^4F_{9/2} \rightarrow {}^4I_{15/2}$ red emission of Er^{3+} ions (predominant) and the $^1G_4 \rightarrow {}^3F_4$ red emission of Tm^{3+} (negligible) ions together.

Here, the $Ba_3Sc_{1.58}F_{12}$:0.4Yb^{3+}, 0.01Er^{3+}, 0.01Tm^{3+} products show blue, green and red emissions, so that white light emission could be produced on the basis of the color superposition principle. The tunable colors were obtained through adjusting the ratio of $Yb^{3+}/Er^{3+}/Tm^{3+}$ in $Ba_3Sc_2F_{12}$ host crystal. We have synthesized a series of $Ba_3Sc_{2(0.795-x)}F_{12}$:0.4$Yb^{3+}$, 0.01$Er^{3+}$, 2$x$$Tm^{3+}$ crystals doped with different Tm^{3+} concentrations (x = 0.0014–0.0030). The up conversion photoluminescence emission spectra of $Ba_3Sc_{2(0.795-x)}F_{12}$:0.4$Yb^{3+}$, 0.01$Er^{3+}$, 2$x$$Tm^{3+}$ are displayed in Fig. 11a.

It is observed that the UC emission spectra of $Ba_3Sc_{2(0.795-x)}F_{12}$:0.4$Yb^{3+}$, 0.01$Er^{3+}$, 2$x$$Tm^{3+}$ crystal consists of blue emission at 482 nm ($^1G_4 \rightarrow {}^3H_6$ of Tm^{3+}), green emission at 520/542 nm ($^2H_{11/2}/{}^4S_{3/2} \rightarrow {}^4I_{15/2}$ of Er^{3+}) and red emission at 648 nm ($^4F_{9/2} \rightarrow {}^4I_{15/2}$ of Er^{3+}). As the concentration of Tm^{3+} increases from 0.0014 to 0.0030, the red emission increases compared to the green emission, which indicates that there is an interaction between Tm^{3+} and Er^{3+}. The resonant cross-relaxation process of $^1G_4$ (Tm^{3+}) + $^4I_{15/2}$ (Er^{3+}) $\rightarrow$ $^3F_4$ (Tm^{3+}) + $^4F_{9/2}$ (Er^{3+}) possibly achieved (Fig. 7) because the energy of the $^1G_4 \rightarrow {}^3F_4$ emission matches the excitation of $^4I_{15/2} \rightarrow {}^4F_{9/2}$ exactly.[77,81,82] This would result in greater population of the red emitting level $^4F_{9/2}$ (Er^{3+}) and enhance the red emission intensity (Fig. 11a). Additionally, the corresponding CIE chromaticity coordinates of $Ba_3Sc_{2(0.795-x)}F_{12}$:0.4$Yb^{3+}$, 0.01$Er^{3+}$, 2$x$$Tm^{3+}$ crystals vary from green light region (0.278, 0.373) to blue white light (0.264, 0.221) by changing the Tm^{3+} ions concentration (Fig. 11b). Furthermore, when x = 0.0022, the white light UC

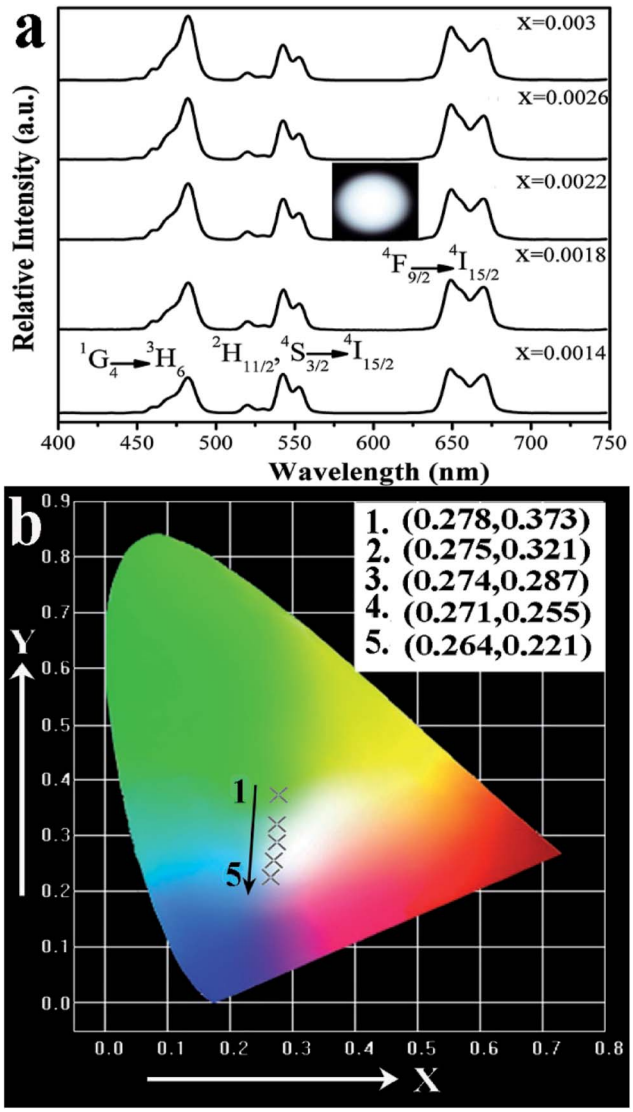

Fig. 11 (a) UC photoluminescence emission spectra of the $Ba_3Sc_{2(0.795-x)}F_{12}$:0.4$Yb^{3+}$, 0.01$Er^{3+}$, 2$x$$Tm^{3+}$ crystals under 980 nm excitation with power density of 3 W cm^{-2}, (b) the corresponding CIE chromaticity coordinates.

photoluminescence in $Ba_3Sc_{1.5856}F_{12}$:0.4Yb^{3+}, 0.01Er^{3+}, 0.0044Tm^{3+} crystal with CIE-x = 0.274 and CIE-y = 0.287 is obtained and the corresponding luminescent photograph also is shown in Fig. 10a for direct observing, which suggests potential applications in display technology and white light sources such as white LEDs.

4. Conclusions

In conclusion, we synthesized $Ba_3Sc_2F_{12}$:Yb^{3+}, Ln^{3+} (Ln = Er, Ho, Tm) crystals through mild hydrothermal route and studied the UC emission properties under 980 nm laser excitation. $Ba_3Sc_2F_{12}$:Yb^{3+}, Ln^{3+} crystals with various shapes and sizes were obtained by selecting different surfactants and controlling pH values. The aspect ratio of the $Ba_3Sc_{2(0.995-x)}F_{12}$:2$x$$Yb^{3+}$, 0.01$Er^{3+}$ crystal increased with the increase of the concentration of the

This journal is © The Royal Society of Chemistry 2017

Open Access Article. Published on 12 December 2017. Downloaded on 6/18/2025 4:16:04 AM.
This article is licensed under a Creative Commons Attribution-NonCommercial 3.0 Unported Licence.

doped Yb^{3+} ions ($x < 0.3$). The blue, green and red up conversion luminescence of the $Ba_3Sc_2F_{12}$:Ln^{3+} system can be attributed to Er^{3+}, Tm^{3+} and Ho^{3+} ions both excited by means of Er^{3+} ground/excited-state absorption and energy transfers from Yb^{3+} ions. Because the back-energy-transfer between Yb^{3+}–Er^{3+} ions could weaken the green emission and increase the population of the red emission $^4F_{9/2}$ level, the enhancement of red emission was obtained with the increase of Yb^{3+} ions. Based on the principle of color superposition, we achieved the white light UC emission with CIE-$x = 0.274$ and CIE-$y = 0.287$ in $Ba_3Sc_{1.5856}F_{12}$:$0.4Yb^{3+}$, $0.01Er^{3+}$, $0.0044Tm^{3+}$ system by controlling the species and concentration of dopants. In view of multicolor UC emission of the $Ba_3Sc_2F_{12}$:Yb^{3+}, Ln^{3+} (Ln = Er, Ho, Tm) systems under 980 nm LD excitation, they may have potential applications in the fields of three dimensional displays, back lighting and white light sources.

Conflicts of interest

There are no conflicts to declare.

Acknowledgements

This project is financially supported by the Fundamental Research Funds for the Central Universities (XDJK2016C147 and XDJK2015B019), the National Natural Science Foundation of China (51302229 and 51302228) and the Scientific Research Foundation for Returned Scholars, Ministry of Education of China (46th).

Notes and references

1 L. Q. Xiong, Z. G. Chen, Q. W. Tian, T. Y. Cao, C. J. Xu and F. Y. Li, *Anal. Chem.*, 2009, **81**, 8687–8694.
2 C. Wang, L. Cheng and Z. Liu, *Theranostics*, 2013, **3**, 317–330.
3 Y. Zhai, C. Zhu, J. Ren, E. Wang and S. Dong, *Chem. Commun.*, 2013, **49**, 2400–2402.
4 H. Kobayashi, M. Ogawa, R. Alford, P. L. Choyke and Y. Urano, *Chem. Rev.*, 2010, **110**, 2620–2640.
5 C. P. Montgomery, B. S. Murray, E. J. New, R. Pal and D. Parker, *Acc. Chem. Res.*, 2009, **42**, 925–937.
6 V. Fernandez-Moreira, F. L. Thorp-Greenwood and M. P. Coogan, *Chem. Commun.*, 2010, **46**, 186–202.
7 J. C. G. Bunzli, *Chem. Rev.*, 2010, **110**, 2729–2755.
8 Q. Zhao, F. Y. Li and C. Huang, *Chem. Soc. Rev.*, 2010, **39**, 3007–3030.
9 Q. Zhao, C. Huang and F. Y. Li, *Chem. Soc. Rev.*, 2011, **40**, 2508–2524.
10 A. Llevot and D. Astruc, *Chem. Soc. Rev.*, 2012, **41**, 242–275.
11 X. Michalet, F. F. Pinaud, L. A. Bentolila, J. M. Tsay, S. Doose, J. J. Li, G. Sundaresan, A. M. Wu, S. S. Gambhir and S. Weiss, *Science*, 2005, **307**, 538–544.
12 J. C. G. Bunzli and C. Piguet, *Chem. Soc. Rev.*, 2005, **34**, 1048–1077.
13 Y. S. Liu, D. T. Tu, H. M. Zhu and X. Y. Chen, *Chem. Soc. Rev.*, 2013, **42**, 6924–6958.
14 J. Zhou, Q. Liu, W. Feng, Y. Sun and F. Y. Li, *Chem. Rev.*, 2015, **115**, 395–465.
15 H. Suzuki, Y. Nishida and S. Hoshino, *Mol. Cryst. Liq. Cryst.*, 2003, **406**, 221–231.
16 Y. P. Li, J. H. Zhang, Y. S. Luo, X. Zhang, Z. D. Hao and X. J. Wang, *J. Mater. Chem.*, 2011, **21**, 2895–2900.
17 K. Z. Zheng, D. S. Zhang, D. Zhao, N. Liu, F. Shi and W. P. Qin, *Phys. Chem. Chem. Phys.*, 2010, **12**, 7620–7625.
18 S. J. Zeng, M.-K. Tsang, C.-F. Chan, K.-L. Wong, B. Fei and J. H. Hao, *Nanoscale*, 2012, **4**, 5118–5124.
19 X. S. Zhai, Y. Wang, X. J. Liu, S. H. Liu, P. P. Lei, S. Yao, S. Y. Song, L. Zhou, J. Feng and H. J. Zhang, *ChemPhotoChem*, 2017, **1**, 369–375.
20 H. L. Li, G. X. Liu, J. X. Wang, X. T. Dong and W. S. Yu, *New J. Chem.*, 2017, **41**, 1609–1617.
21 Z. C. Li, D. C. Zhou, Y. Yang, Y. Gao, P. Ren and J. B. Qiu, *Opt. Mater.*, 2016, **60**, 277–282.
22 B. Zhao, L. Yuan, S. S. Hu, X. M. Zhang, X. J. Zhou, J. F. Tang and J. Yang, *CrystEngComm*, 2016, **18**, 8044–8058.
23 W. Y. Yin, L. J. Zhou, Z. J. Gu, G. Tian, S. Jin, L. Yan, X. X. Liu, G. M. Xing, W. L. Ren, F. Liu, Z. W. Pan and Y. L. Zhao, *J. Mater. Chem.*, 2012, **22**, 6974–6981.
24 Y. S. Liu, D. T. Tu, H. M. Zhu and X. Y. Chen, *Chem. Soc. Rev.*, 2013, **42**, 6924–6958.
25 F. Wang, Y. Han, C. S. Lim, Y. Lu, J. Wang, J. Xu, H. Chen, C. Zhang, M. Hong and X. Liu, *Nature*, 2010, **463**, 1061–1065.
26 B. T. Chen, B. Dong, J. Wang, S. Zhang, L. Xu, W. Yu and H. W. Song, *Nanoscale*, 2013, **5**, 8541–8549.
27 Y. J. Ding, X. Teng, H. Zhu, L. L. Wang, W. B. Pei, J. J. Zhu, L. Huang and W. Huang, *Nanoscale*, 2013, **5**, 11928–11932.
28 W. B. Pei, B. Chen, L. L. Wang, J. S. Wu, X. Teng, R. Lau, L. Huang and W. Huang, *Nanoscale*, 2015, **7**, 4048–4054.
29 Q. M. Huang, J. C. Yu, E. Ma and K. M. Lin, *J. Phys. Chem. C*, 2010, **114**, 4719–4724.
30 C. M. Zhang, P. Ma, C. X. Li, G. G. Li, S. S. Huang, D. M. Yang, M. M. Shang, X. J. Kang and J. Lin, *J. Mater. Chem.*, 2011, **21**, 717–723.
31 L. Rao, W. Lu, T. M. Zeng, Z. G. Yi, H. B. Wang, H. R. Liu and S. J. Zeng, *J. Mater. Chem. B*, 2014, **2**, 6527–6533.
32 T. Q. Sheng, Z. L. Fu, X. J. Wang, S. H. Zhou, S. Y. Zhang and Z. W. Dai, *J. Phys. Chem. C*, 2012, **116**, 19597–19603.
33 L. P. Jia, Q. Zhang and B. Yan, *Mater. Res. Bull.*, 2014, **55**, 53–60.
34 L. Lei, D. Q. Chen, F. Huang, Y. L. Yu and Y. S. Wang, *J. Alloys Compd.*, 2012, **540**, 27–31.
35 H. X. Guan, Y. Sheng, Y. H. Song, K. Y. Zheng, C. Y. Xu, X. M. Xie, Y. Z. Dai and H. F. Zou, *RSC Adv.*, 2016, **6**, 73160–73169.
36 P. Zhang, Y. Y. He, J. H. Liu, J. Feng, Z. Q. Sun, P. P. Lei, Q. H. Yuan and H. J. Zhang, *RSC Adv.*, 2016, **6**, 14283–14289.
37 S. Sarkar, B. Meesaragandla, C. Hazra and V. Mahalingam, *Adv. Mater.*, 2013, **25**, 856–860.
38 I. Etchart, M. Bérard, M. Laroche, A. Huignard, I. Hernández, W. P. Gillin, R. J. Curryd and A. K. Cheetham, *Chem. Commun.*, 2011, **47**, 6263–6265.
39 B. Zhao, D. Y. Shen, J. Yang, S. S. Hu, X. J. Zhou and J. F. Tang, *J. Mater. Chem. C*, 2017, **5**, 3264–3275.

Open Access Article. Published on 12 December 2017. Downloaded on 6/18/2025 4:16:04 AM.
This article is licensed under a Creative Commons Attribution-NonCommercial 3.0 Unported Licence.

40 M. N. Mayakovaa, S. V. Kuznetsova, V. V. Voronova, A. E. Baranchikovb, V. K. Ivanovb and P. P. Fedorov, *Russ. J. Inorg. Chem.*, 2014, **59**, 773–777.
41 P. Gredin, A. D. Kozitk and M. Qnacton, *Z. Anorg. Allg. Chem.*, 1993, **619**, 1088–1094.
42 Y. Fei, S. L. Zhao, X. Sun, L. H. Huang, D. G. Deng and S. Q. Xu, *J. Non-Cryst. Solids*, 2015, **428**, 20–25.
43 X. Teng, Y. H. Zhu, W. Wei, S. C. Wang, J. F. Huang, R. Naccache, W. B. Hu, A. L. Y. Tok, Y. Han, Q. C. Zhang, Q. Y. Fan, W. Huang, J. A. J. Capobianco and L. Huang, *J. Am. Chem. Soc.*, 2012, **134**, 8340–8343.
44 H. X. Mai, Y. W. Zhang, R. Si, Z. G. Yan, L. D. Sun, L. P. You and C. H. Yan, *J. Am. Chem. Soc.*, 2006, **128**, 6426–6436.
45 B. Shao, Z. Yang, Y. Wang, J. Li, J. Yang, J. Qiu and Z. Song, *ACS Appl. Mater. Interfaces*, 2015, **7**, 25211–25218.
46 J. Liao, Z. Yang, H. Wu, D. Yan, J. Qiu, Z. Song, Y. Yang, D. Zhou and Z. Yin, *J. Mater. Chem. C*, 2013, **1**, 6541–6546.
47 F. Wang, R. Deng, J. Wang, Q. Wang, Y. Han, H. Zhu, X. Chen and X. Liu, *Nat. Mater.*, 2011, **10**, 968–973.
48 S. H. Fan, S. K. Wang, H. T. Sun, S. Y. Sun, G. J. Gao and L. L. Hu, *J. Am. Ceram. Soc.*, 2017, **100**, 3061–3069.
49 S. H. Fan, S. K. Wang, H. T. Sun, S. Y. Sun, G. J. Gao and L. L. Hu, *Opt. Express*, 2017, **25**, 180–190.
50 S. H. Hua, G. J. Gao, D. Busko, Z. Q. Lin, S. K. Wang, X. Wang, S. Y. Sun, A. Turshatov, B. S. Richards, H. T. Sun and L. L. Hu, *J. Mater. Chem. C*, 2017, **5**, 9770–9777.
51 G. J. Gao, D. Busko, S. Kauffmann-Weiss, A. Turshatov, L. A. Howard and B. S. Richards, *J. Mater. Chem. C*, 2017, **5**, 11010–11017.
52 G. J. Gao, A. Turshatov, L. A. Howard, D. Busko, R. Joseph, D. Hudry and B. S. Richards, *Advanced Sustainable Systems*, 2017, **1**, 1600033.
53 G. G. Li, M. M. Shang, D. L. Geng, D. M. Yang, C. Peng, Z. Y. Cheng and J. Lin, *CrystEngComm*, 2012, **14**, 2100–2111.
54 D. Q. Chen, Y. S. Wang, Y. L. Yu, P. Huang and F. Y. Weng, *J. Solid State Chem.*, 2008, **181**, 2763–2767.
55 A. Kumari and V. K. Rai, *Mater. Res. Bull.*, 2015, **72**, 168–175.
56 Y. J. Ding, X. X. Zhang, H. Zhu and J. J. Zhu, *J. Mater. Chem. C*, 2014, **2**, 946–952.
57 D. Q. Chen, Y. L. Yu, F. Huang, A. P. Yang and Y. S. Wang, *J. Mater. Chem.*, 2011, **21**, 6186–6192.
58 Z. H. Xu, X. J. Kang, C. X. Li, Z. Y. Hou, C. M. Zhang, D. M. Yang, G. G. Li and J. Lin, *Inorg. Chem.*, 2010, **49**, 6706–6715.
59 B. Zhao, L. Yuan, S. S. Hu, X. M. Zhang, X. J. Zhou, J. F. Tang and J. Yang, *New J. Chem.*, 2016, **40**, 9211–9222.
60 J. Prywer, *Prog. Cryst. Growth Charact. Mater.*, 2005, **50**, 1–38.
61 Y.-W. Jun, J.-H. Lee, J.-S. Choi and J. Cheon, *J. Phys. Chem. B*, 2005, **109**, 14795–14806.
62 L. Zhu, L. Qin, X. D. Liu, J. Y. Li, Y. F. Zhang, J. Meng and X. Q. Cao, *J. Phys. Chem. C*, 2007, **111**, 5898–5903.
63 Z. J. Miao, Z. M. Liu, K. L. Ding, B. X. Han, S. D. Miao and G. M. An, *Nanotechnology*, 2007, **18**, 125605.
64 C. X. Li, J. Yang, Z. W. Quan, P. P. Yang, D. Y. Kong and J. Lin, *Chem. Mater.*, 2007, **19**, 4933–4942.
65 A. Huignard, V. Buissette, G. Laurent, T. Gacoin and J. P. Boilot, *Chem. Mater.*, 2002, **14**, 2264–2269.
66 C. X. Li, C. M. Zhang, Z. Y. Hou, L. L. Wang, Z. W. Quan, H. Z. Lian and J. Lin, *J. Phys. Chem. C*, 2009, **113**, 2332–2339.
67 S. H. Yu, B. Liu, M. S. Mo, J. H. Huang, X. M. Liu and Y. T. Qian, *Adv. Funct. Mater.*, 2003, **13**, 639–647.
68 Y. Gao, Q. Zhao, Z. H. Xu and Y. G. Sun, *New J. Chem.*, 2014, **38**, 2629–2638.
69 C. F. Liu, C. K. Zhang, H. Q. Song, C. P. Zhang, Y. G. Liu, X. H. Nan and G. Z. Cao, *Nano Energy*, 2016, **22**, 290–300.
70 X. F. Wu, W. Wang, N. N. Song, X. J. Yang, S. Khaimanov and N. Tsidaeva, *Chem. Eng. J.*, 2016, **306**, 328–392.
71 R. Swaminathan, M. A. Willard and M. E. McHenry, *Acta Mater.*, 2006, **54**, 807–816.
72 L. B. Tahar, L. S. Smiri, M. Artus, A.-L. Joudrier, F. Herbst, M. J. Vaulay, S. Ammar and F. Fiévet, *Mater. Res. Bull.*, 2007, **42**, 1888–1896.
73 P. Shikha, T. S. Kang and B. S. Randhawa, *J. Alloys Compd.*, 2015, **625**, 336–345.
74 N. Niu, P. P. Yang, Y. C. Liu, C. X. Li, D. Wang, S. L. Gai and F. He, *J. Colloid Interface Sci.*, 2011, **362**, 389–396.
75 H. B. Wang, W. Lu, T. M. Zeng, Z. G. Yi, L. Rao, H. R. Liu and S. J. Zeng, *Nanoscale*, 2014, **6**, 2855–2860.
76 D. L. Gao, X. Y. Zhang, H. R. Zheng and E. J. He, *J. Alloys Compd.*, 2013, **554**, 395–399.
77 J. Yang, C. M. Zhang, C. Peng, C. X. Li, L. L. Wang, R. T. Chai and J. Lin, *Chem.–Eur. J.*, 2009, **15**, 4649–4655.
78 G. Glaspell, J. Anderson, J. R. Wilkins and M. S. Ei-Shall, *J. Phys. Chem. C*, 2008, **112**, 11527–11531.
79 Z. F. Shan, D. Q. Chen, Y. L. Yu, P. Huang, F. Y. Weng, H. Lin and Y. S. Wang, *Mater. Res. Bull.*, 2010, **45**, 1017–1020.
80 L. P. Tu, X. M. Liu, F. Wu and H. Zhang, *Chem. Soc. Rev.*, 2015, **44**, 1331–1345.
81 D. Q. Chen, Y. S. Wang, K. L. Zheng, T. L. Guo, Y. L. Yu and P. Huang, *Appl. Phys. Lett.*, 2007, **91**, 251903.
82 B. Dong, H. W. Song, H. Q. Yu, H. Zhang, R. F. Qin, X. Bai, G. H. Pan, S. Z. Lu, F. Wang, L. B. Fan and Q. L. Dai, *J. Phys. Chem. C*, 2008, **112**, 1435–1440.

 This journal is © The Royal Society of Chemistry 2017